RADIATION RESEARCH **191**, 383–397 (2019)
0033-7587/19 $15.00
©2019 by Radiation Research Society.
All rights of reproduction in any form reserved.
DOI: 10.1667/RR15130.1

Cardiac and Renal Delayed Effects of Acute Radiation Exposure: Organ Differences in Vasculopathy, Inflammation, Senescence and Oxidative Balance

Joseph L. Unthank,[a,b] Miguel Ortiz,[a] Hina Trivedi,[e] Louis M. Pelus,[c] Carol H. Sampson,[d] Rajendran Sellamuthu,[d] Alexa Fisher,[d] Hui Lin Chua,[d] Artur Plett,[d] Christie M. Orschell,[b,d] Eric P. Cohen[e] and Steven J. Miller[a,b,1]

Departments of [a] Surgery, [b] Cellular and Integrative Physiology, [c] Microbiology and Immunology and [d] Medicine, Indiana University School of Medicine, Indianapolis, Indiana, and [e] Department of Medicine, University of Maryland School of Medicine, Baltimore, Maryland

Unthank, J. L, Ortiz, M., Trivedi, H., Pelus, L. M., Sampson, C. H., Sellamuthu, R., Fisher, A., Chua, H. L., Plett, A., Orschell, C. M., Cohen, E. P. and Miller, S. J. Cardiac and Renal Delayed Effects of Acute Radiation Exposure: Organ Differences in Vasculopathy, Inflammation, Senescence and Oxidative Balance. *Radiat. Res.* 191, 383–397 (2019).

We have previously shown significant pathology in the heart and kidney of murine hematopoietic-acute radiation syndrome (H-ARS) survivors of 8.7–9.0 Gy total-body irradiation (TBI). The goal of this study was to determine temporal relationships in the development of vasculopathy and the progression of renal and cardiovascular delayed effects of acute radiation exposure (DEARE) at TBI doses less than 9 Gy and to elucidate the potential roles of senescence, inflammation and oxidative stress. Our results show significant loss of endothelial cells in coronary arteries by 4 months post-TBI (8.53 or 8.72 Gy of gamma radiation). This loss precedes renal dysfunction and interstitial fibrosis and progresses to abnormalities in the arterial media and adventitia and loss of coronary arterioles. Major differences in radiation-induced pathobiology exist between the heart and kidney in terms of vasculopathy progression and also in indices of inflammation, senescence and oxidative imbalance. The results of this work suggest a need for different medical countermeasures for multiple targets in different organs and at various times after acute radiation injury to prevent the progression of DEARE. © 2019 by Radiation Research Society

INTRODUCTION

The risk of exposure to debilitating and lethal doses of radiation is increasing as a result of nuclear arms proliferation, potential terrorist attacks and natural disasters at nuclear power plants. Long-time survivors of acute high-dose exposure can develop delayed effects of acute radiation exposure (DEARE) in multiple organ systems. Cardiovascular and renal disease are two manifestations of DEARE that have been studied clinically and experimentally at targeted radiation exposures $\geq$10 Gy. Cardiovascular disease has been identified as a major cause of death in survivors of atomic bombs and nuclear accidents (*1–6*). Radiation nephropathy is associated with cardiovascular disease after total-body irradiation (TBI) (*6, 7*), and has been shown to cause myocardial and coronary vascular disease after local as well as total-body exposures (*8, 9*), suggesting a causal link between the renal and cardiovascular DEARE.

Although radiation doses at significantly less than 10 Gy may raise the risk of cardiovascular disease in both humans and animal models (*2, 4, 10*), there is a paucity of information related to the time course of cardiovascular disease progression, the specific mechanisms which mediate the progression of vasculopathy, and their association with renal disease. Chronic inflammation and persistent oxidative stress are considered to have major roles in the development of DEARE in multiple organs (*11, 12*), and are believed by some to be due to radiation-induced damage to vascular endothelium. The vascular endothelium is generally considered to be one of the most radiation-sensitive non-hematopoietic tissues in the body (*13*) and to have a role in multiple organ injury (*14, 15*) after radiation exposure. Endothelial cell senescence can be induced by ionizing radiation through an NF-κB-dependent pathway (*16*), leading to oxidative stress and inflammation, which results in cardiovascular disease and fibrosis (*17*). Vascular injury is thus not only a marker of radiation exposure but also a mechanism for delayed tissue injury in multiple organs (*13*). However, there are few studies addressing such mechanisms of DEARE at doses less than 10 Gy and a causative role of inflammation and oxidative stress has been challenged, especially for radiation nephropathy (*18, 19*).

Editor's note. The online version of this article (DOI: 10.1667/RR15130.1) contains supplementary information that is available to all authorized users.

[1] Address for correspondence: Department of Surgery Division of Vascular Surgery, Indiana University School of Medicine, Joseph E. Walther Hall (R3), 980 W. Walnut St., C647 Indianapolis, IN 46202; email: sjmiller@iupui.edu.

We have recently reported development of DEARE in the heart and kidney of murine survivors in an established hematopoietic-acute radiation syndrome (H-ARS) model (*20*). In mice that received 8.7–9.0 Gy TBI, we observed significant pathology in the heart and kidney, including coronary arterial fibrosis, renal glomerulosclerosis, loss of tubules and interstitial fibrosis. The goal of the current study was to determine temporal relationships in the development of vasculopathy and the progression of renal and cardiovascular DEARE in our murine H-ARS model at TBI doses less than 9 Gy, and to elucidate the potential roles of senescence, inflammation and oxidative stress.

MATERIALS AND METHODS

Mouse Irradiation and Husbandry

All studies followed the PHS Policy on Humane Care and Use of Laboratory Animals, were compliant with animal welfare guidelines as reviewed by AAALAC and were approved by the Indiana University School of Medicine Institutional Animal Care and Use Committee.

Specific pathogen-free C57BL/6 mice (50/50 male/female; Jackson Laboratory, Bar Harbor, ME) were received at 10 weeks of age and acclimated for two weeks prior to irradiation. Mice were placed in single chambers of a Plexiglas® irradiation apparatus and received a single uniform total-body dose of 8.53 or 8.72 Gy of gamma radiation ($LD_{50/30}$ and $LD_{70/30}$, respectively) from a ^{137}Cs radiation source (0.95–1.00 Gy/min). Mice were identified by ear punch, and husbandry and health status monitoring were performed as described elsewhere (*21*). These mice had been used as vehicle controls in survival studies. Although the DEARE studies used both male and female mice, group sizes were not sufficient to allow statistical analyses of potential differences due to sex. Survivors of the acute phase (30 days) were used in the current studies of DEARE along with age-matched nonirradiated control mice. Separate groups of mice were used for histological and molecular studies of kidney and heart at time points from 4 to 22 months post-TBI (Supplementary Table S1; http://dx.doi.org/10.1667/RR15130.1.S1). Blood urea nitrogen (BUN) was determined for mice from both groups at all time points.

Tissue Harvest, Fixation and Histological Staining

Mice were anesthetized via isoflurane inhalation, the thoracic cavity was opened and blood was collected from the left ventricle for preparation of serum. Mice from which tissues were used for histological and morphometric analysis were perfusion fixed via the left ventricle at 100–120 mm Hg. The mice were first perfused with phosphate buffered saline (PBS) including vascular dilator (0.1 m*M* adenosine and 0.01 m*M* sodium nitroprusside). This was followed by 10% neutral buffered formalin (NBF). After perfusion-fixation, the heart and right kidney were placed in NBF for storage until processing. Tissues collected for qPCR analysis were obtained from separate groups of mice and excised from the animal immediately after perfusion with PBS and dilator. After this perfusion, the heart apex and one half of the right kidney were placed in RNA preservation solution and stored at –20°C until RNA purification. Formalin-fixed tissues were paraffin embedded, sectioned, then stained with hematoxylin and eosin (H&E), Periodic acid-Schiff and hematoxylin (PASH), picrosirius red (PSR) or Perls' Prussian blue.

Imaging, Histological Scoring and Morphometric Analysis

Imaging. Digital images of kidney and heart sections were acquired using Leica Application Suite imaging software using a Leica DM 5000B microscope (Leica Microsystems Inc., Buffalo Grove, IL) with a Leica DMC 4500 digital camera. Multiple sections (4–5) from each mouse were evaluated for histopathological characteristics. Morphometric measurements were performed using ImageJ Software (National Institutes of Health, Bethesda, MD).

Blood urea nitrogen. BUN was determined in mouse serum as described elsewhere (*20*).

Renal histopathological analyses. A quantitative scoring system of radiation-induced renal histopathological changes previously developed for quantitative assessment of radiation nephropathy in rats and adapted by one of the coauthors for this murine model (*20, 22*) was used to assess glomerulosclerosis and interstitial fibrosis, the two primary manifestations of radiation nephropathy observed in this model (*20*). PASH-stained tissues were used to identify sclerosed glomeruli. A glomerulus was identified as sclerosed if 50% or more of the glomerular tufts lacked evenly dispersed nuclei or capillaries and showed an increase in matrix deposition. At least 20 random glomeruli per mouse were assessed using ImageJ. The percentage of sclerosed glomeruli for each mouse was calculated and a numerical scale was developed from the percentage data. A numerical scale for interstitial fibrosis in the renal cortex was also developed based on qualitative descriptors. Renal cortex fibrosis was also assessed from PSR-stained sections as described elsewhere by Farris *et al*. (*23*).

Arterial histopathology analyses. Arterial wall characteristics in heart and kidney sections including the area and thickness of the media and adventitia, and intimal and medial cell nuclear number and density, were performed using H&E stained sections as described elsewhere (*24, 25*). Relative collagen content in the adventitia and media of the left coronary artery was also determined with thresholding to identify the area of PSR staining (*26*). Threshold analysis was performed using the green channel of the RGB stack, and a grayscale value of 60 was used as the threshold to standardize values between animals.

Microvascular injury and hemosiderin deposition. The presence of Perls' Prussian blue-positive regions or distinct areas (nodes) was evaluated in heart and kidney cross sections and the total number of nodes (heart) or the total Perls'-positive area (kidney) was calculated.

Immunohistochemical Analyses

Immunohistochemistry. Antigens were detected in paraffin-embedded tissues using the VECTASTAIN® Elite ABC-HRP Kit (Vector® Laboratories, Burlingame, CA) and the Vector DAB Peroxidase (HRP) Substrate Kit with standard protocols. Antigen retrieval was performed by immersing the slides in citrate buffer (0.01 *M*, pH 6.0) preheated via microwave oven for 45 s, followed by heating for 3×5 min at 50% power, replenishing the buffer as needed between intervals. Tissue sections were blocked with 1× protein blocking solution (Vector Animal-free Blocker) and normal goat serum (1:50 dilution) for 60 min. Primary antibodies were diluted with the protein blocking solution and incubated overnight at 4°C in a hydration chamber. Antibodies included: anti-smooth muscle α-actin (D-SMA, rabbit polyclonal, 1:400; Millipore, Temecula, CA), and macrophage marker F4-80 (1:20; Abcam®, San Francisco, CA). Secondary antibodies were diluted 1:50 in protein blocker plus appropriate serum, and incubation was performed for 60 min at room temperature. The slides were briefly counterstained with Gill's 3 hematoxylin, dehydrated through graded alcohols to xylene and coverslipped with a permanent mounting medium prior to imaging.

Cardiac and renal arteriole density. For arteriolar density determination in heart and kidney, smooth muscle α-actin-positive vessels were detected as described in the immunohistochemical methods, and arterioles were verified morphologically by wall thickness; arteriole tunica media thickness was greater than in venules, and capillaries (<10 μm) were α-actin-negative. Arteriolar density was quantified by counting all arterioles 10 to 25 μm in diameter in 100× images of five serial tissue sections/mouse. Arteriole numbers

TABLE 1
Wall Characteristics of Coronary Arteries

	Nonirradiated, age-matched controls				TBI			
Time post-TBI:	4 months	6 months	13 months	18 months	4 months	6 months	13 months	18 months
No. intimal nuclei	19.5 ± 2.28	20.3 ± 3.04	20.4 ± 2.30	24.7 ± 0.44	11.3 ± 1.18	14.5 ± 2.39	9.9 ± 1.83	10.3 ± 1.28
Luminal diameter (μm)	133 ± 12.1	140 ± 15.7	123 ± 11.4	155 ± 11.3	138 ± 12.5	162 ± 6.2	143 ± 13.2	159 ± 14.3
Luminal perimeter (μm)	417 ± 37.9	510 ± 49.4	386 ± 35.8	485 ± 35.5	434 ± 39.3	510 ± 19.4	449 ± 41.6	499 ± 35.5
No. medial nuclei	18.2 ± 3.96	16.4 ± 1.82	13.9 ± 0.83	20.2 ± 0.44	14.4 ± 2.93	16.8 ± 2.77	12.7 ± 2.18	13.5 ± 2.81
Medial area (μm^2)	4,090 ± 591	4,440 ± 705	4,300 ± 486	7,676 ± 1,274	3,980 ± 807	5,680 ± 430	5,580 ± 597	7,620 ± 1,844
Medial thickness (μm)	9.66 ± 0.56	9.93 ± 0.62	10.5 ± 0.63	15.6 ± 1.66	8.67 ± 0.96	11.1 ± 0.58	12.2 ± 0.76	14.6 ± 2.20
Medial collagen (μm^2)	536 ± 60	1,164 ± 91	1,133 ± 73	2,250 ± 384	1,108 ± 269	1,829 ± 218	2,422 ± 362	4,297 ± 845
Adventitial collagen (μm^2)	1,462 ± 120	1,612 ± 169	2,875 ± 235	4,599 ± 909	2,341 ± 250	2,374 ± 236	3,986 ± 1,445	5,712 ± 813

Notes. Individual mouse averages were obtained from two cross sections of the left coronary artery. n = 4 for each group and time from 4–13 months post-TBI; n = 3 for nonirradiated and n = 5 for TBI at 18 months post-TBI.

for each section were normalized to the tissue area and values are expressed as animal means.

Cardiac macrophages. Macrophages were detected as described in the immunohistochemical methods, and cells positive for the F4/80 macrophage-specific antigen were quantified in images of tissue sections of the entire left ventricle using an average of 16 fields/section/mouse at 200×. Macrophage numbers are expressed as means normalized to the image field area.

Molecular Expression Analyses

Renal and cardiac real-time PCR. Relative differences between TBI and nonirradiated mouse heart and kidney mRNA expression were determined using reverse transcription real-time quantitative PCR (RT-qPCR). Total RNA isolation and reverse transcription (1.0 μg of RNA) for samples of heart apex and right kidney were performed as described elsewhere (*20*). For PCR, cDNA (5.0 μl, 1:50 dilution) was combined with primers and probes for Nox2, Nox4, p47phox, $p16^{INK4a}$ or hypoxanthine guanine phosphoribosyl transferase (HPRT) endogenous control (TaqMan® Gene Expression Assays; Applied Biosystems®, Foster City, CA) in the presence of a PCR master mix (FastStart Universal Probe Master Mix; Roche Applied Science, Indianapolis, IN). Reactions were run in triplicate on an Applied Biosystems 7500 Real-Time PCR System using relative quantification ($^{\Delta\Delta}$Ct) with standard two-step 7500 PCR cycling conditions (40 cycles). Differences in PCR product yields between groups were determined by comparing the fold differences between target mRNA after normalization to HPRT.

RESULTS

General Mouse Data

For all experiments, mouse body masses for all time points post-TBI ranged from 19.0–41.6 g for the irradiated mice and 23.0–55.8 g for age-matched nonirradiated mice. Specific group/time data are shown in the Supplementary Table S1 (http://dx.doi.org/10.1667/RR15130.1.S1).

DEARE in Heart

The presence of DEARE in heart was assessed by determining multiple wall characteristics of coronary arteries using morphometric analyses (*24, 25*); these characteristics, summarized in Table 1, included intimal and medial cell nuclear numbers, luminal perimeters, medial areas and collagen-positive areas in the media and peri-arterial space. Representative images of cross sections of coronary arteries from TBI and control age-matched nonirradiated mice used for these analyses are shown in Supplementary Figs. S1 and S2 (http://dx.doi.org/10.1667/RR15130.1.S1).

Collagen deposition. The area of PSR staining in cross sections of the largest coronary arteries was quantified to assess collagen content in the media and adventitia (Supplementary Fig. S1; http://dx.doi.org/10.1667/RR15130.1.S1). Medial collagen area averaged over all time points was significantly greater in the TBI compared to nonirradiated mice (2,429 ± 335 vs. 1,271 ± 340 μm^2, $P = 0.021$), and medial collagen (as percentage of total medial area) increased significantly with age in the TBI but not nonirradiated (Fig. 1A) group. The age-related increase in medial collagen appeared to be associated with gaps between adjacent vascular smooth muscle cells which were confirmed by smooth muscle α-actin staining (Supplementary Fig. S1) and were especially apparent at 18 months post-TBI. PSR staining in the adventitia and peri-arterial area between the arterial media and adjacent cardiac myocytes was not different between TBI and nonirradiated mice (3,604 ± 397 μm^2 vs. 2,637 ± 402 μm^2, $P = 0.098$) but was increased with age in both groups (Fig. 1B). Focal regions of myocardial interstitial fibrosis and increased pericardial fibrosis were not observed, in contrast to what

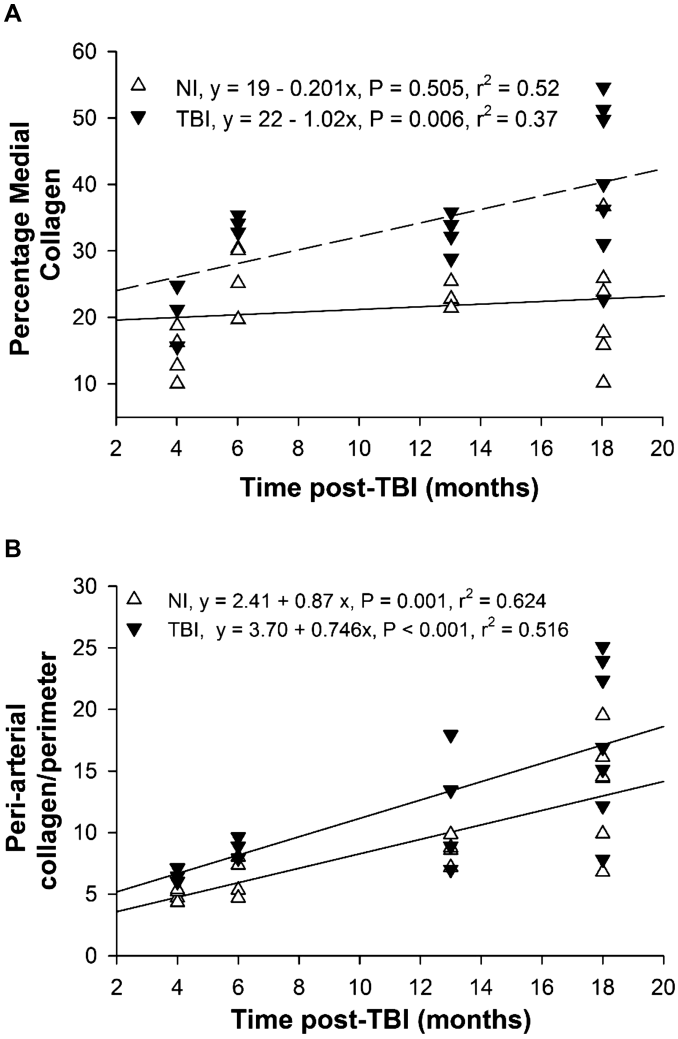

FIG. 1. Collagen in left coronary arteries. Averages in individual TBI and nonirradiated mice are shown for the percentage of the arterial media (panel A) and peri-arterial space normalized to luminal perimeter (panel B) stained with PSR. A significant increase with time was observed in medial collagen of TBI but not in nonirradiated mice, and in peri-arterial collagen in both TBI and nonirradiated mice. Averages are from two arterial sections for each mouse. n = 4–7 per group.

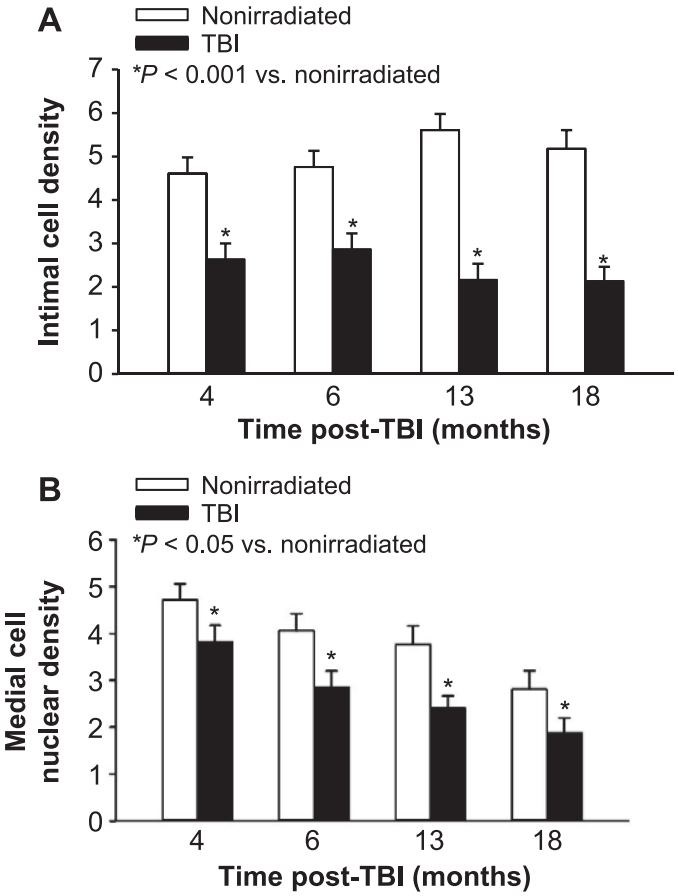

FIG. 2. Intimal and medial cell nuclear density in left coronary arteries. Panel A: Intimal cell nuclear density (average number of intimal nuclei per 100 μm luminal perimeter) in the largest coronary arteries is shown for all time points post-TBI and in age-matched, nonirradiated controls. Two-way ANOVA testing showed that intimal nuclear density was significantly less in TBI mice compared to nonirradiated mice at all time points ($P < 0.001$) but no differences were observed between time points in either the TBI or nonirradiated groups. Panel B: Medial cell nuclear density (average number of medial nuclei per 1,000 μm^2 medial area) in the largest coronary arteries is shown for all time points post-TBI and in nonirradiated controls. Two-way ANOVA showed that medial nuclear density was significantly less in TBI mice compared to nonirradiated mice at all time points ($P = 0.004$). Medial cell nuclear density decreased with time ($y = 3.96 - 0.121x$, $P < 0.001$, $r^2 = 0.613$ for TBI vs. $y = 7.76 - 0.104x$, $P = 0.056$, $r^2 = 0.252$ for nonirradiated controls) with a significant difference between 4 and 18 months in the TBI mice. n = 4 for each group and time from 4–13 months post-TBI; n = 3 nonirradiated and 5 TBI mice for 18 months.

we previously reported (*20*). However, the mice in the previously experiments were studied at a longer time post-TBI and at higher radiation doses (872–904 cGy), which may account for the different results in the current study.

Intimal and medial cell density in coronary arteries. Representative images of coronary arterial cross sections used for determining intimal perimeter, medial area and intimal and medial cell nuclear numbers and density are shown in Supplementary Fig. S2. The intimal cell numbers per coronary arterial cross section of all nonirradiated and TBI mice were 21.2 ± 1.06 and 11.5 ± 0.99 (Table 1, $P < 0.001$), respectively. This 50% reduction of cell number after irradiation was present from the earliest (4 months) through the latest (18 months) time post-TBI. All the coronary artery intimal cell nuclei were histologically characteristic of endothelial cell nuclei and no intimal reactivity for F4/80 or smooth muscle α-actin was observed. The reduced number of intimal cell nuclei in the TBI group was not due to a reduction in coronary artery size because the luminal diameters and perimeters of the coronary arteries were similar (Table 1) and because normalization of intimal cell number to luminal perimeter also indicated 50% reduction at all times post-TBI (2.45 ± 0.180 in the TBI compared to 5.04 ± 0.192 in the age-matched nonirradiated group, $P < 0.001$; Fig. 2A).

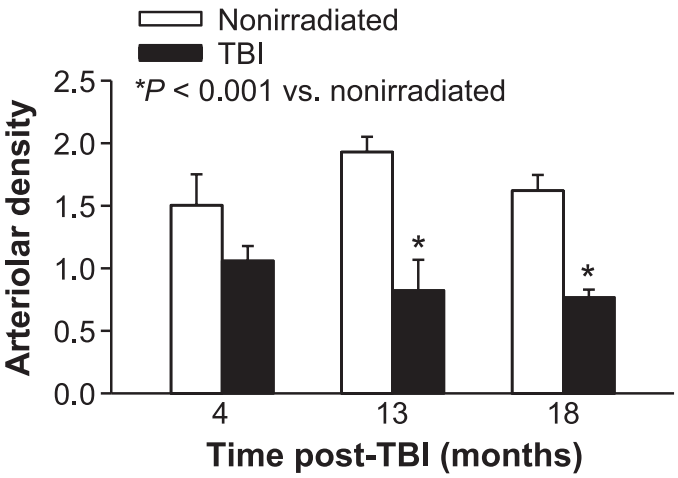

FIG. 3. Left ventricle arteriolar density. Loss of myocardial arterioles post-TBI was assessed in left ventricle tissue sections by quantifying α-actin-positive vessels 10–25 μm in diameter in TBI and age-matched nonirradiated mice. Arterioles were counted in five tissue sections/mouse at the various time points and normalized to the myocardial tissue area (arterioles/1 × 10^5 μm^2). n = 4 mice for 4, 13 months; n = 6–7 mice for 18 months.

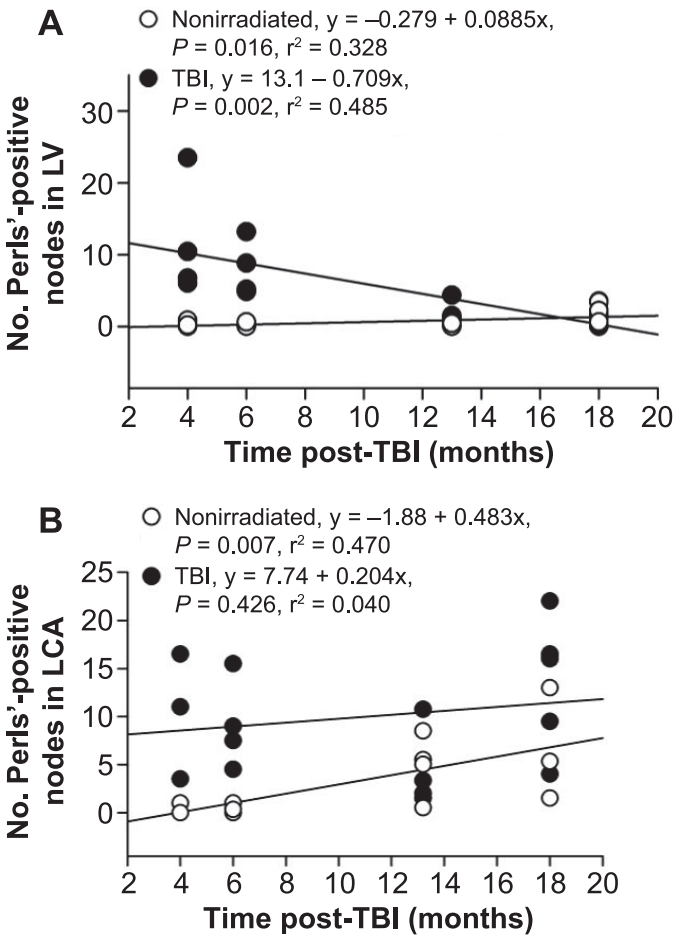

FIG. 4. Hemosiderin (Perls' Prussian Blue stain) in left ventricle (LV). Panel A: Average number of distinct Perls'-positive regions (nodes) in individual nonirradiated and TBI mice. Each individual point represents the average from a minimum of five 400× fields. In nonirradiated mice, a slight but significant increase was observed. A significant and progressive decrease with time post-TBI occurred in the myocardium of the TBI mice. Panel B: Number of distinct Perls'-positive nodes in left coronary arteries of individual TBI and nonirradiated mice. For each mouse, counts from coronary arteries in two cross sections were averaged. The number of nodes were greater ($P < 0.001$) in TBI mice at all time points except 13 months. Unlike the myocardium, the number of hemosiderin deposits did not decrease in the TBI coronary arteries. There was a progressive increase in Perls' staining in the coronary arteries of nonirradiated mice. n = 3–4 for nonirradiated and 4–6 for TBI mice.

Unlike the intima, no significant decrease was observed in the number of medial cell nuclei in arterial cross sections of TBI compared to nonirradiated mice. The averages for all time points for medial cell nuclear numbers in the coronary arteries of nonirradiated and TBI groups were 17.2 ± 1.35 and 14.3 ± 1.27, respectively ($P = 0.140$). Medial cell nuclear density (number of nuclei divided by medial area) averaged over all time points was lower in TBI than nonirradiated mice (2.72 ± 0.208 vs. 3.69 ± 0.222, $P = 0.004$) as shown in Fig. 2B. The medial nuclear counts included all nuclei without consideration of the cell type or if smooth muscle cells were binuclear (see Supplementary Fig. S2). The decline in medial cell density appears to result from expansion of the media with collagen deposition rather than cell loss or smooth muscle hypertrophy.

Coronary arteriolar rarefaction. Arteriolar density in the left ventricle myocardium was determined by α-SMA positive arterioles (Supplemental Fig. S3; http://dx.doi.org/10.1667/RR15130.1.S1). Arteriolar density in the irradiated mice tended to be decreased at 4 months compared to that of nonirradiated mice (30%, $P = 0.08$) and was significantly less (>50%, $P < 0.001$) at 13 and 18 months post-TBI (Fig. 3).

Hemosiderin and microvascular injury. Perls' Prussian blue stain was utilized to evaluate iron deposition as an index of microvascular injury and hemorrhage, as previously reported elsewhere in locally irradiated hearts (*27*). Perls'-positive regions were consistently observed in the pericardium, myocardium and coronary arteries of the left ventricle in TBI mice (see Supplementary Fig. S4; http://dx.doi.org/10.1667/RR15130.1.S1). In the irradiated mice, the number of pericardial/myocardial Perls'-positive regions or nodes was greatest at 4 months post-TBI and progressively decreased, as shown in Fig. 4A. Perls'-positive nodes were also seen in the medial and adventitia wall areas of the coronary arteries. Perls'-positive nodes were much more common in the left coronary arteries of irradiated compared to nonirradiated mice, as shown in Fig. 4B. Although the number of Perls' nodes in nonirradiated left coronary arteries increased with age, irradiated mice had significantly more Perls'-positive nodes than did nonirradiated control mice at all time points post-TBI except 13 months. However, the number of nodes in and around the coronary arteries of TBI mice did not decrease with time. The nodes

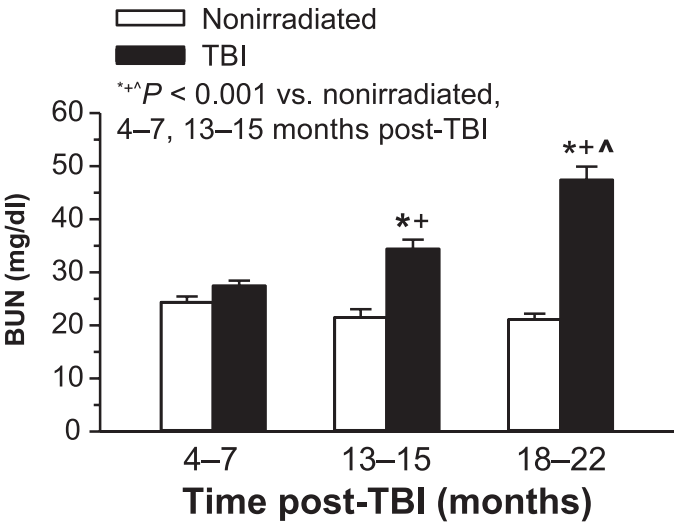

FIG. 5. Blood urea nitrogen (BUN) in nonirradiated and TBI mice. BUN was significantly elevated in TBI vs. age-matched nonirradiated controls at 13–15 months (n = 12 nonirradiated; n = 10 TBI) and 18–22 months (n = 8 nonirradiated; n = 9 TBI), but not at 4–7 months (n = 16 nonirradiated; n = 18 TBI).

of hemosiderin were primarily seen in the wall and peri-arterial area of the large coronary arteries, but were also occasionally seen in smaller arteries and arterioles.

DEARE in Kidney

The gold standard for radiation nephropathy is histopathology, and radiation-induced histopathological injury correlates closely with renal function assessed by blood urea nitrogen (BUN) in rodents (*20, 28*). Both BUN and histopathology showed the development of renal DEARE in the H-ARS survivors analyzed in this study.

Renal function. BUN significantly increased over time in irradiated mice (Fig. 5). No age-related elevation of BUN was observed in the nonirradiated control mice.

Renal cortex pathology. The most apparent histological abnormalities in kidneys of TBI mice are glomerulosclerosis and interstitial fibrosis (*20*). The results presented in Table 2 show a progressive injury with both irradiation and aging. A more quantitative assessment of glomerular and interstitial fibrosis of renal cross sections stained with PSR (Supplementary Fig. S5; http://dx.doi.org/10.1667/RR15130.1.S1) was performed with morphometric methods similar to those described by Farris *et al*. (*23*). Increased PSR staining was apparent at 18 months in both nonirradiated and TBI mice and was most obvious in the glomeruli of the TBI mice. Quantification of the area stained for collagen indicated a progressive increase in both nonirradiated and TBI mice (Fig. 6). Relative to 6 months for nonirradiated mice, the area of the renal cortex that stained positive for collagen was increased 1.5-fold and threefold at 18 months in nonirradiated and TBI mice, respectively.

Renal arterial pathology. The abnormalities of the intima and media that were readily apparent in the coronary arteries were not seen in the renal arteries (Supplementary Fig. S6; http://dx.doi.org/10.1667/RR15130.1.S1). Intimal cell density in renal arteries of irradiated mice averaged 7.49 ± 1.01 nuclei per 100 μm luminal perimeter at 18 months post-TBI compared to 9.63 ± 0.09 in nonirradiated, age-matched controls. This lack of effect on endothelial cells in the renal arteries is consistent with previously published studies in which it was reported that radiation-induced vascular injury in the kidney is primarily limited to the glomeruli (*29, 30*).

Renal arteriolar density. Quantification of kidney arterioles showed an 18–26% reduction in mean number in TBI compared to nonirradiated mice at the three time points examined, but the difference was statistically significant only at 18 months post-TBI (Fig. 7 and Supplementary Fig. S7; http://dx.doi.org/10.1667/RR15130.1.S1). No significant change in arteriole number was detected with age in the nonirradiated mice.

Hemosiderin deposition in kidney. In the irradiated mice, Perls'-positive staining was observed primarily in tubules of the outer cortex (Supplementary Fig. S8; http://dx.doi.org/10.1667/RR15130.1.S1). The regions stained with Perls' were more diffuse than in the heart and the staining appeared less intense. The area stained positively in high-powered fields was quantified and plotted in Fig. 8. Perls' staining appeared to be elevated at 4 months post-TBI, reduced to near nonirradiated values in most TBI mice at 6 months (3 of 4) and then again elevated in 50% of the mice (5 of 10) at 13 to 18 months post-TBI. The mice with the greatest degree of renal Perls' staining also had the highest BUN levels. In the kidney, Perls' staining was not observed around large arteries or arterioles as was observed in the heart.

TABLE 2
Renal Function and Histopathology

	Nonirradiated, age-matched controls				TBI			
Time post-TBI:	4 months	6 months	13 months	18 months	4 months	6 months	13 months	18 months
Sclerosed glomeruli	0.00	0.00	0.00	1.00	0.00	0.25	0.50	0.71
Interstitial fibrosis	0.00	0.00	0.50	1.00	0.33	0.50	1.00	1.57
Total score	0.00	0.00	0.50	2.00	0.33	0.75	1.50	2.28
Average BUN	25	23	27	23	31	27	36	54

Notes. Histopathologic scores and BUN values were determined as described in Materials and Methods. n = 4 for each group and time from 4–13 months post-TBI; n = 3 for nonirradiated and 5 for TBI at 18 months post-TBI.

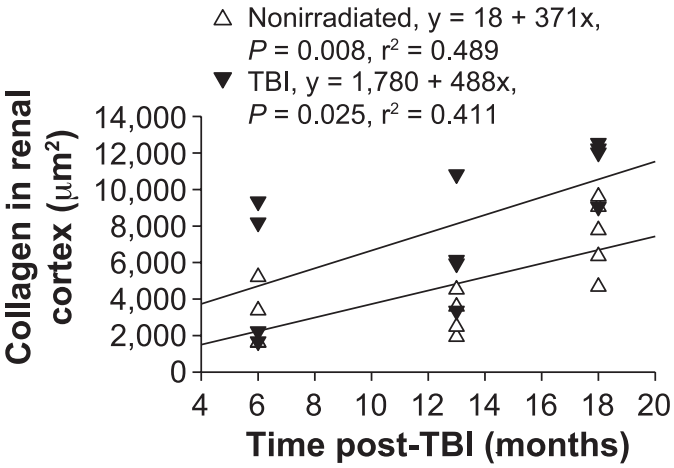

FIG. 6. Collagen area in the renal cortex. Average area stained with PSR in renal cross sections of individual nonirradiated and TBI mice. Each point represents an average of a minimum of eight images of the renal cortex acquired at 400×. Collagen area increased with age in both groups.

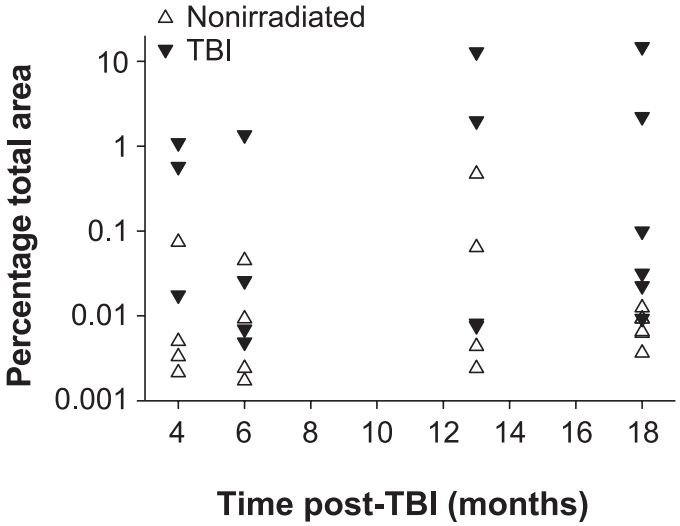

FIG. 8. Hemosiderin (Perls' Prussian blue) in the renal cortex. Individual averages are expressed as percentage total area for nonirradiated and TBI mice at 4, 6, 13 and 18 months post-TBI. The overall average was 0.041 ± 0.0003% for nonirradiated vs. 2.06 ± 0.016% ($P = 0.004$ by ANOVA). Post hoc comparisons indicated significance between nonirradiated and TBI at 18 months ($P = 0.029$). n = 3 for 4 months, TBI; n = 6 for 18 months, nonirradiated and TBI; n = 4 for all other time points.

Senescence, Inflammation and Oxidative Balance

Based on apparent differences observed in radiation-induced vasculopathy in the heart and kidney, further analyses were performed to identify the basic mechanisms that might be responsible for these divergent histological alterations. To this end, we evaluated p16^{INK4a} and NADPH oxidase subunit expression by qPCR to assess senescence and oxidative balance, and F4/80 by immunostaining to evaluate the presence of macrophages/inflammation, as described below.

Heart and kidney senescence. Potential induction of stress-induced cellular senescence due to TBI was assessed in both heart and kidney by determining relative expression changes of p16^{INK4a} mRNA. A small but significant increase in p16 expression was seen 7 months post-TBI in heart but not in kidney (Fig. 9A). In contrast, at 22 months p16 expression was significantly increased in kidney, but not heart (Fig. 9B). Relative fold changes for p16 at the two time points were higher in kidney (~8×) than in heart (~2×). An analysis of age effects on p16 expression in nonirradiated mice indicated that relative to 7-month-old controls, p16 increased threefold in kidney and ~5-fold in heart at subsequent time points (data not shown). Thus, while p16 expression increased with age, radiation exposure caused an additional increase in cell senescence, with the exception of heart at 22 months post-TBI.

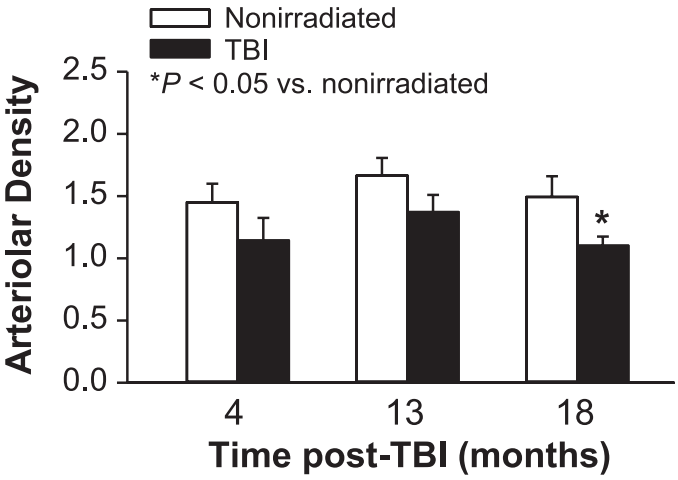

FIG. 7. Renal arteriolar density in TBI and nonirradiated mice. Arterioles (α-actin positive vessels 10–25 μm in diameter) were counted in five sections per mouse and normalized to the kidney tissue section area (arterioles/1 × 10^5 μm^2). n = 4 mice for 4 and 13 months; n = 6–7 mice for 18 months.

Inflammation. The presence of macrophages in heart and kidney was determined as an index of radiation-induced inflammation. Assessment of F4/80-positive cells in myocardium indicated an apparent increase post-TBI at 4 months (Supplementary Fig. S9A and B; http://dx.doi.org/10.1667/RR15130.1.S1). The majority were located in the interstitial space between myocytes, and not in the vascular wall or in the perivascular space. Quantification of myocardial F4/80-positive cells indicated that their number was significantly increased at 4 months post-TBI (~8×), then declined by 13 months, although still elevated at that time compared to age-matched nonirradiated controls (Fig. 10). By 18 months post-TBI myocardial macrophage number was not different from numbers in nonirradiated control tissues. No increase with aging was detected, as macrophage numbers in nonirradiated mice did not vary over time. In contrast to heart, the kidney had almost no detectable macrophages (Supplementary Fig. S9C; http://dx.doi.org/10.1667/RR15130.1.S1).

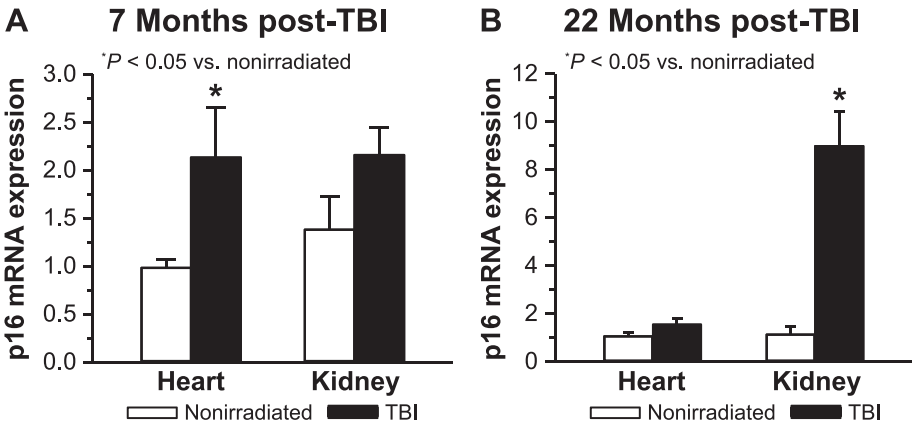

FIG. 9. Assessment of radiation-induced cardiac and renal senescence. Relative expression changes for $p16^{INK4a}$ mRNA were determined by real-time qPCR in heart and kidney tissues at (panel A) 7 months (n = 5–6) and (panel B) 22 months (n = 3–5) post-TBI and compared to age-matched nonirradiated tissues. Results are expressed as relative fold change after normalization to HPRT.

NADPH oxidase (Nox) subunit expression. Our previously published analysis of Nox2 mRNA expression in heart showed increases at 9 and 21 months post-TBI relative to nonirradiated controls (*20*), suggesting a contribution of Nox to radiation-mediated abnormal reduction/oxidation balance. In the current study, Nox2 subunit mRNA expression, along with p47phox and Nox4, was determined in both heart and kidney. Significantly increased expression of all three Nox subunits relative to nonirradiated control tissue was detected in heart 7 months post-TBI (Fig. 11A), but not kidney (Fig. 11C). However, at 22 months post-TBI only cardiac Nox4 was significantly increased relative to nonirradiated tissue (Fig. 11B). In kidney, only p47phox expression was elevated at 22 months post-TBI relative to nonirradiated control tissue (Fig. 11D).

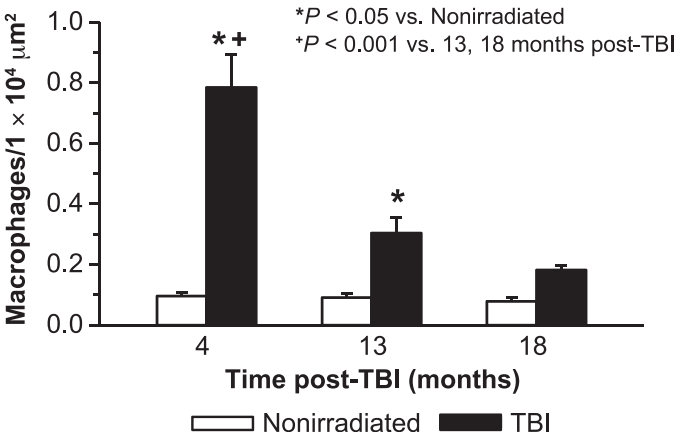

FIG. 10. Assessment of cardiac inflammation. The presence of macrophages was determined in TBI and age-matched nonirradiated mouse heart left ventricle myocardium. Macrophage numbers/unit area were determined by counting F4/80-positive cells in 16 fields/section/mouse (200×) of heart tissue sections and normalizing to unit area. n = 4 for 4 and 13 months, nonirradiated and TBI; n = 4 for 18 months, nonirradiated; n = 7 for 18 months, TBI).

DISCUSSION

The results of our study in murine H-ARS survivors of less than 9 Gy TBI demonstrate the presence of significant vasculopathy by 4 months post-TBI. A major aspect of the early vasculopathy is the loss of coronary endothelial cells. This loss precedes renal dysfunction and interstitial fibrosis and is followed by abnormalities in the arterial media and adventitia and loss of intramyocardial arterioles.

Major differences exist between the heart and kidney in terms of vasculopathy and also in indices of inflammation, senescence and oxidative imbalance. Such differences in pathobiology suggest a need for different medical countermeasures for multiple targets in different organs and at different times after acute radiation injury.

Loss of Coronary Artery Intimal Cells before Significant Renal Dysfunction

Our results demonstrate a significant loss of endothelial cells in coronary arteries that occurred by four months post-TBI and persisted through 18 months post-TBI (Fig. 2A and Supplementary Fig. S2; http://dx.doi.org/10.1667/RR15130.1.S1). This aspect of cardiovascular DEARE occurred before the development of renal dysfunction, as assessed by elevated blood urea nitrogen which is not significantly elevated until 13 months post-TBI in this model.

This loss of coronary arterial endothelial cells in our study is consistent with earlier reported studies of the effects of higher doses of radiation on the arterial endothelium. In locally irradiated canine femoral arteries (cumulative dose >30 Gy), Fonkalsrud *et al.* (*31*) reported the earliest manifestation of radiation injury to occur in the endothelium. This injury included disruption of the nuclei and localized sloughing of endothelial cells within 48 hours. While repopulation of the intima occurred, the surface remained irregular with incomplete coverage. In a review of arterial injury resulting from therapeutic radiation, Himmel

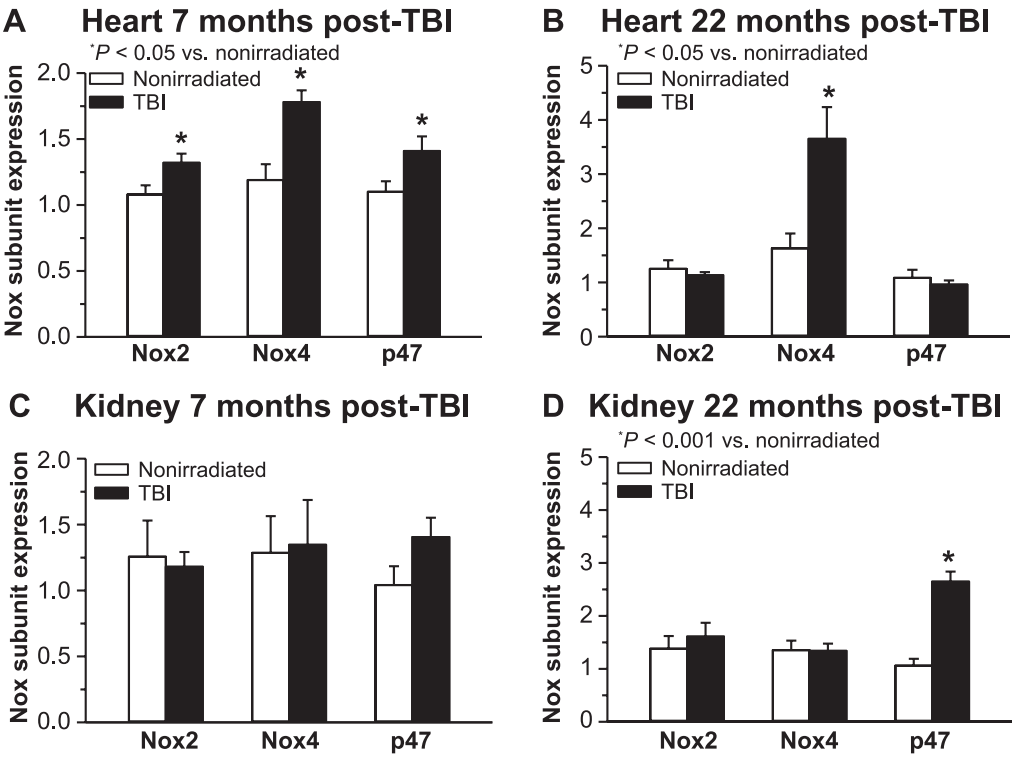

FIG. 11. Nox subunit expression changes postirradiation. Changes in Nox subunit mRNA expression were assessed by real-time qPCR as an indicator of oxidative balance in heart and kidney of TBI mice at 7 months (panels A and C) and 22 months (panels B and D) post-TBI relative to age-matched nonirradiated controls. Results are expressed as relative fold change after normalization to HPRT. n = 4–6 mice for all groups.

and Hassett (*32*) reported the earliest changes to be characterized by swelling and vacuolation of the endothelial cytoplasm and subsequent nuclear fragmentation. More recently in an experimental rat model with local irradiation of the heart (15–20 Gy at 1.95 Gy/min), Boerma *et al*. (*33*) reported endothelial cell loss in coronary arteries. The relatively early radiation-induced loss of coronary arterial endothelial cells, which precedes renal dysfunction, is consistent with a fundamental role of the endothelium in DEARE (*14, 15*),

Progression of Radiation-Induced Coronary Arterial/ Arteriolar Pathology

In addition to the loss of endothelial cells, coronary arteries from our murine H-ARS survivors exhibited a progressive increase in percentage medial collagen and decrease in medial cell nuclear density (Figs. 1A and 2B, respectively), which may result in loss of autoregulation as well as thrombosis and ischemic injury.

Our observations of medial fibrosis in coronary arteries postirradiation are consistent with previously studies of human arteries and experimental models. Himmel and Hassett reported degeneration of smooth muscle cells and replacement by collagen to be a late effect in human arteries exposed to therapeutic radiation (*32*). After local irradiation of canine femoral arteries, Fonkalsrud *et al*. (*31*) observed late medial effects including focal necrosis and dense fibrosis. Boerma *et al*. (*33*) reported smooth muscle cell loss and medial and adventitial fibrosis in rat coronary arteries after local irradiation.

We also observed significant injury in small coronary arterioles in the TBI mice. A significant loss (>50%) of small arterioles (≤25 μm) occurred by 13 months post-TBI (Fig. 3). To our knowledge, this is the first report of such a radiation effect at TBI doses <9 Gy. Microvascular rarefaction induced by ionizing radiation has been previously reported in experimental models in rabbits, rats and mice (*8, 27, 34, 35*). Myocardial capillary density indices were found to be reduced after local irradiation of the heart at doses ≥10 Gy in rats and rabbits (*34, 35*) with the effect at 10 Gy being transient (*34*). Seeman *et al*. (*27*) observed a dose- and time-dependent alteration in microvascular density (CD31-positive vessels up to ~15 μm diameter) after local irradiation in mice. They reported a transient increase at doses of 2 and 8 Gy, but not after 16 Gy at 20 weeks postirradiation. Reductions in myocardial microvascular density of ~25%, were observed at 40 weeks in 16 Gy irradiated mice and at 60 weeks in 9 Gy irradiated mice. Baker *et al*. (*8*) observed a 32% decrease in the density of small coronary arterioles 4 months postirradiation in rats that were treated with 10 Gy TBI followed by bone marrow transplantation but not in rats that received local 10 Gy irradiation to the heart.

Our results of a >50% reduction in coronary arteriolar density at 13 months after 8.5 Gy TBI are consistent with the dose- and time-dependent effects of radiation on vascular injury (*13*).

The progressive vasculopathy observed in the coronary arteries and arterioles is associated with reduced endothelial nitric oxide synthase expression (*8*), senescence (*17*) and denudation [Fig. 1A and as reported by Boerma *et al*. (*33*)]. As BUN elevation was coincident with the later coronary arterial vasculopathy, renal disease may also have been a contributing factor (*6, 9*). The arteriolar injury and loss add to the larger arterial injury, and are likely to cause an ischemic cardiomyopathy. We did not have myocardial function studies to confirm that, however.

Perls' Prussian Blue and Hemosiderin

We observed hemosiderin deposits in the heart and kidney of our murine H-ARS survivors. In the heart, hemosiderin was observed as small focal deposits in the epicardium, myocardium, arterial wall and perivascular space. Hemosiderin in the kidney was more diffuse and located primarily in renal tubules. The focal deposits in the heart are consistent with those reported by Seemann *et al*. (*34*) of iron-containing macrophages in the epicardium and myocardium at 5 months after local heart irradiation at 8 Gy and 10 months after 2 and 8 Gy. Preliminary data (not shown) from experiments co-localizing Perls' and F4/80 staining, along with morphological assessment, indicated that at least 40% of the Perls' staining in heart was associated with iron-containing macrophages. The hemosiderin observed in renal tubules is consistent with a process reported by Alfrey *et al*. (*36–38*) that occurs after glomerular injury; increased capillary permeability results in leakage of transferrin followed by the dissociation of iron in the acidic tubular fluid and then iron absorption by the tubular cells.

Because the Perls' staining of tubules also could indicate the presence of lipofuscin, additional staining with the AFIP method was performed. Results (not shown) indicated variable intensity of AFIP lipofuscin staining in limited areas of the kidney tubules at 18 months post-TBI, but not at earlier time points. Similar results were seen in heart, with minimal AFIP lipofuscin staining detectable only at 18 months and staining did not correlate with areas positive for Perls'. Further work is warranted with an alternative technique to investigate the potential presence of lipofuscin at earlier times post-TBI.

While Cohen *et al*. (*18*) demonstrated that the iron chelator deferiprone did not mitigate radiation-induced nephropathy, additional studies are warranted to determine if hemosiderin, such as observed in our murine model, is simply an indication of vascular injury or if there is some degree of radiation-induced iron-mediated injury, especially to endothelium (*39, 40*), that could be mitigated by appropriate therapies. Serum iron elevation has been reported in humans (*41*) and mice (*42, 43*) post-TBI, and could act through reactive oxygen species (ROS) to injure the vasculature and induce heart and kidney disease (*36, 44, 45*). Thus, serum iron and its relationship to development of DEARE-related pathology and dysfunction also deserves further study.

Renal Arterial and Arteriolar Injury Less than Observed in Heart

The prominent vascular effects of endothelial cell loss, medial degeneration and fibrosis in the coronary arteries was not seen in renal arteries, and renal arteriolar density was only significantly reduced at 18 months post-TBI (Fig. 7). This suggests that these renal vessels are less sensitive to radiation injury than similar-sized coronary vessels, consistent with a published review of *in vivo* endothelial cell sensitivity to radiation injury (*46*). This hypothesis is supported by studies showing coronary vessel injury from 8–16 Gy delivered locally or by TBI and studies in the kidney which have reported the rarity of renal arterial and arteriolar injury by locally delivered single radiation doses from 9.8 Gy in pigs (*30*) and 11–19 Gy in mice (*29*). This contrasts with the glomular capillaries, which have distinct injury after local irradiation and TBI at doses ≥10 Gy (*47*).

Contrast of Heart And Kidney DEARE: Senescence, Inflammation and Redox Imbalance

Senescence. Based on the results of our histological analyses, as well as previously published studies showing evidence of radiation-induced inflammation and oxidant stress, we sought to determine whether stress-induced senescence occurred in heart and kidney. Our results demonstrated a significant increase in heart senescence as assessed by $p16^{INK4a}$ expression as early as 7 months post-TBI. In contrast, significant increases in kidney p16 did not occur until 22 months post-TBI compared to nonirradiated mice.

While cellular senescence is a consequence of aging, irradiation may lead to stress-induced premature senescence in tissues, including heart (*48*). An early increase in senescence is significant because it is associated with decreased vascular function as well as increased oxidant stress, NF-κB activation, and inflammation (*17*). Several studies using moderate to high doses of radiation have shown induction of senescence in cultured endothelial cells from a variety of tissues (*17*), but much less is known *in vivo*. Recent evidence indicates induction of cardiac endothelial cell senescence after local heart X-ray irradiation at 8 or 16 Gy (*49*), and 6 Gy TBI results in a small increase in senescent cells in heart (*50*). The early increase in p16 we detected in heart appears to be similar in extent to that shown in geriatric mice (*51*), and thus is consistent with stress-induced early senescence and the notion that radiation exposure induces a state of accelerated aging (*52*) (see Fig. 12). The reason for the delayed p16 increase in kidney is

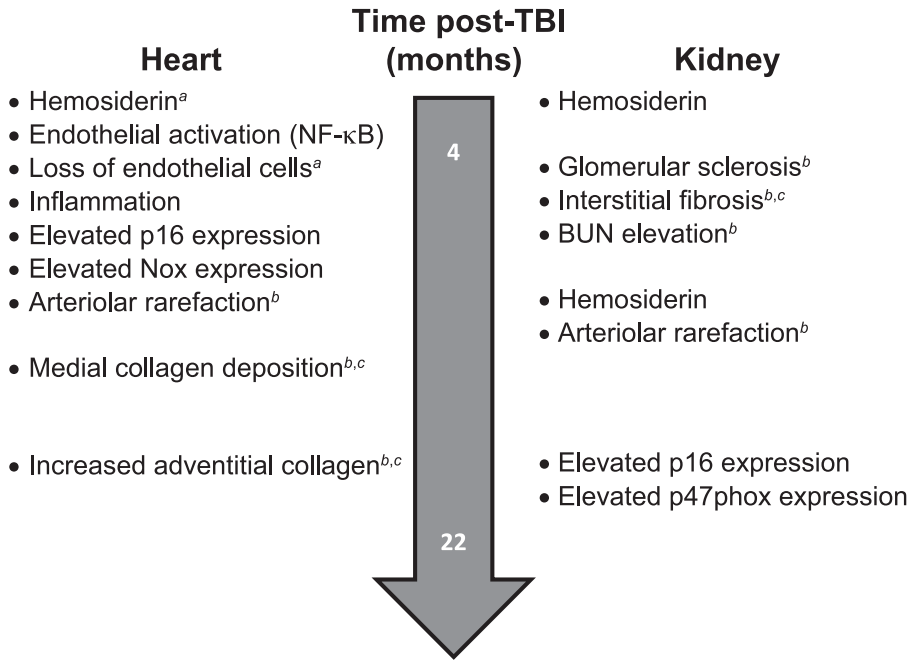

FIG. 12. Approximate timeline for DEARE progression from 4 to 22 months post-TBI for the various described pathophysiologies in heart vs. kidney. Those that were [a]persistent, [b]progressive or [c]consistent with accelerated aging are noted in the figure.

unclear, but correlates with the time scale of onset of pathology development as well as the elevation of BUN. Future work is needed to confirm senescence with additional markers such as beta galactosidase, to examine earlier time points and to identify the specific cell types involved.

Inflammation. Our results with mouse heart showed an early, highly significant increase in myocardial macrophages with a decrease by 13 months post-TBI, then a decline to control numbers by 18 months. In contrast, macrophages were essentially undetectable in kidney post-TBI, even at 4 months.

Inflammation is thought to be a major contributor to the development of cardiovascular disease, including fibrosis (*11, 48*). An early and sustained inflammatory response postirradiation has been suggested as a primary mechanism for development of long-term vasculopathy (*53*). Our results in heart are consistent with the role of inflammation in the development of cardiovascular DEARE, and suggest increased numbers of macrophages function as an early event to initiate subsequent development of cardiac pathologies. The observation of few macrophages in kidney is consistent with studies in other models suggesting a limited role for radiation-mediated inflammation in kidney (*54, 55*).

Redox imbalance. Because redox imbalance and resultant oxidant stress has been shown to be associated with inflammation and senescence after irradiation, we evaluated NADPH oxidase (Nox) expression changes in our mouse tissues post-TBI. The current results showed differential tissue and temporal Nox expression changes, with all Nox subunits increased in heart, but not kidney, at 7 months post-TBI. Differential expression occurred at 22 months post-TBI, with Nox4 elevated in heart and p47phox in kidney. These kidney data are consistent with previously published studies showing no role for oxidant stress-induced damage up to 17 weeks postirradiation (*18*).

Elevated ROS production occurs within milliseconds of radiation exposure (*56*), but little is known about the role of persistent, ongoing oxidant stress in DEARE, especially in the cardiovascular system. The role of chronic persistent oxidative stress is much discussed but not well proven (*18, 19, 57*). A primary source of ROS in vasculature is NADPH oxidase (Nox), which is present in various isoforms. While Nox activity is necessary for normal vascular redox signaling function (*58–60*), its expression is increased in arterial disease and overexpression is associated with oxidant stress, vascular dysfunction and pathology (*61–63*). We previously showed an increase in Nox2 mRNA expression associated with cardiovascular DEARE post-TBI at $<$10 Gy (*20*), and the current data extend these results to p47phox and Nox4 in heart and kidney.

Since the p47phox subunit is a key regulator of Nox2 activity, it is possible that Nox2 may be a source of ROS in kidney at the later time point even though its expression was not altered. However, elevated ROS at 22 months after irradiation may be a result, rather than a cause, of pathological changes. Overexpression of Nox2 in endothelium has been linked with increased cardiac fibrosis and inflammation in the context of renin-angiotensin activation

(*64*). Nox4 is important for normal kidney function and is also associated with renal dysfunction and disease (*65*), but our results do not suggest a significant role for Nox4 in kidney post-TBI. Senescent endothelial cells produce increased levels of ROS, due in part to Nox, and the early elevated Nox4 detected in heart is consistent with the early increase in $p16^{INK4a}$ expression. Elevated Nox4 has been shown to be associated with senescence in murine hematopoietic stem cells 8 weeks after 6.5 Gy TBI (*66*). Nox4 also is thought to be a primary source of hydrogen peroxide, which is associated with cardiovascular disease in humans (*67*). Thus, Nox4-derived peroxide may be an important source of ROS in heart to investigate at both early and late DEARE time points, as it may participate both in initiation and sustainment of oxidant stress. Increased Nox also have been linked to mitochondrial oxidant stress (*68*) as well as NF-κB activation (*69*), consistent with current results. Further studies are needed to provide cellular localization of specific Nox subunits in irradiated mice, and to determine the ability of Nox ablation or inhibitors to prevent the development of cardiovascular DEARE.

In conclusion, these studies have determined the temporal relationships in the development of vasculopathy and the progression of renal and cardiovascular DEARE and presence of markers of senescence, inflammation and redox imbalance in a murine H-ARS model at survivable TBI doses of <9 Gy (Fig. 12). Our findings demonstrate that radiation doses near the $LD_{50/30}$ in H-ARS result in: 1. progressive renal and cardiovascular DEARE; 2. early vascular injury, especially in the heart, with loss of endothelial cells and associated with tissue iron accumulation; 3. progressive vasculopathy characterized by loss of arterioles and fibrosis of media and perivascular space; and 4. organ differences in radiation-induced tissue senescence, inflammation and oxidative imbalance. These results provide important insight regarding potential mitigators and appropriate times for their administration.

SUPPLEMENTARY INFORMATION

The supplementary information includes representative images of heart and kidney histology as well as immunohistochemistry that are relevant to the data presented in the figures.

Table S1. Mouse gender and body mass data. Separate sets of mice were used for experiments related to histology/immunohistochemistry and quantitative PCR. Groups within these categories are presented as months post-TBI, and individual data for gender and body mass (g) are given for all age-matched nonirradiated and TBI mice.

Fig. S1. Representative images of coronary artery cross sections stained with PSR (top 4 panels) and α-smooth muscle actin (bottom 4 panels) from TBI and nonirradiated age-matched control mice at 4 and 18 months post-TBI. The peri-arterial PSR staining increased with time in both nonirradiated and TBI mice, whereas medial PSR staining increased only in the TBI mice. Immunohistochemical staining of coronary artery cross sections with α-smooth muscle actin demonstrated gaps between adjacent vascular smooth cells in mice at 18 months post-TBI that were not observed at earlier time points. These results suggest that late effects of TBI include medial expansion due to collagen deposition. All images were acquired at 400×; scale bar = 50 μm.

Fig. S2. Representative images (400×) of H&E stained left coronary artery cross sections from TBI and nonirradiated age-matched control mice at 4 and 18 months post-TBI. Arrows indicate the location of intimal nuclei, which were reduced in number in the TBI mice at all ages. There was no apparent decrease in the number of medial cell nuclei. The intimal cell nuclei were all consistent with an endothelial phenotype. Some of the medial cells were binucleate (see asterisk), an indication of senescence.

Fig. S3. Representative images (400×) of α-actin-positive arterioles in TBI and age-matched nonirradiated myocardium at 13 months post-TBI. Images were acquired from formalin-fixed paraffin-embedded sections of heart reacted with an antibody to α-smooth muscle cell actin, as described in Materials and Methods, and used to determine arteriolar density. Arteriole numbers per unit area in the left ventricle of TBI mice decreased significantly at 13 months compared to nonirradiated controls, and similar results were obtained at 18 months post-TBI.

Fig. S4. Representative images of left ventricle and coronary artery cross sections stained with Perls' Prussian blue from TBI and age-matched nonirradiated control mice at 4 months post-TBI, and additional TBI tissues at 6 and 18 months. All images were acquired at 400×. Perls'-positive regions (hemosiderin deposits) were observed in the myocardium and coronary arteries of TBI mice. Sites of deposition included the myocardium and epicardium and, in arteries, the peri-arterial space, medial layer and intima.

Fig. S5. Representative images of the renal cortex stained with PSR in TBI and age-matched nonirradiated control mice at 6, 13 and 18 months postirradiation. All images were acquired at 400×; scale bar = 50 μm (shown in the panel labeled 18 months nonirradiated) applies to all images. Increased PSR staining in the renal cortex was observed first in the glomeruli of TBI mice and later (18 months) in the interstitium, especially in regions of tubular atrophy.

Fig. S6. Representative images of PSR (top 4 panels; 400×) and H&E stained cross sections (bottom 2 panels) of renal arteries from TBI and age-matched nonirradiated control mice. Fewer renal arteries were available for analysis than coronary arteries as not all kidney sections were obtained at the location which contained these arteries. In the PSR-stained sections, some renal arteries from TBI mice appeared to have more collagen in the adventitia and media at later times post-TBI; however, there was significant variation within and between mice of both the nonirradiated and TBI groups. As shown in the H&E

stained sections (bottom 2 panels), no striking differences were observed in intimal cell nuclear number for either large arteries or arterioles, contrary to what was observed in the heart.

Fig. S7. Representative images (400×) of α-actin positive arterioles in TBI and age-matched nonirradiated renal cortex at 18 months. Images were acquired from formalin-fixed paraffin embedded sections of kidney reacted with an antibody to α-smooth muscle cell actin as described in Materials and Methods and used to determine arteriolar density. A decrease in arteriole number per unit area was significant only at 18 months post-TBI.

Fig. S8. Representative images of kidney cross sections stained with Perls' Prussian blue from TBI and age-matched nonirradiated control mice. Perls' staining was significantly elevated in the renal cortex of most irradiated mice at 4 months post-TBI, was reduced to near-nonirradiated values in most TBI mice at 6 months (3 of 4) and then became elevated in 50% of the mice (5 of 10) at 13–18 months post-TBI. Perls' staining was observed primarily in the tubules of the superficial cortex region, but not all tubules within a region exhibited staining. Staining was also observed in some glomeruli at later time points. Perls' positive staining or deposits of hemosiderin were not observed in the renal arteries, even when the arteries were surrounded by tubules with hemosiderin.

Fig. S9. Representative images (400×) of macrophages in cross sections of heart and kidney reacted with the F4/80 antibody. Panel A: Age-matched nonirradiated mouse heart left ventricle had an extremely low macrophage density. Panel B: Four-months post-TBI, mouse heart left ventricle demonstrated a significantly increased number of macrophages (arrows) compared to nonirradiated controls. Panel C: Renal macrophages were essentially undetectable at any time point in nonirradiated kidney sections and only occasionally in TBI tissue (shown here are images at 4 months post-TBI).

ACKNOWLEDGMENTS

We thank Supriya Chittajallu for her expert assistance with the BUN and qPCR experiments. This project was funded in whole or in part with federal funds from the National Institute of Allergy and Infectious Diseases and National Institute on Aging (both of the National Institutes of Health, Department of Health and Human Services) under NIAID contract nos. HHSN266200500043C and HHSN272201000046C, NIAID grant nos. 1U01AI107340-01 and 2R44 AI088288-03A1 and NIA grant no. R01AG046246-01. Further support was provided by the Department of Defense under grants PR140896, PR141527, and PR140433P1. This work has also been supported in part by resources and the use of facilities at the Baltimore VAMC (made available to EPC).

Received: May 7, 2018; accepted: February 26, 2019; published online: March 22, 2019

REFERENCES

1. Preston DL, Shimizu Y, Pierce DA, Suyama A, Mabuchi K. Studies of mortality of atomic bomb survivors. Report 13: Solid cancer and noncancer disease mortality: 1950–1997. Radiat Res 2003; 160:381–407.
2. Belyi D, Kovalenko A, Bazyka D. Acute radiation syndrome survivors after chernobyl accident: History of irradiation, diagnostic mistakes and death reasons in long-term period. Radiat Emerg Med 2013; 2:5–12.
3. Ozasa K, Shimizu Y, Suyama A, Kasagi F, Soda M, Grant EJ, et al. Studies of the mortality of atomic bomb survivors, report 14, 1950–2003: An overview of cancer and noncancer diseases. Radiat Res 2012; 177:229–43.
4. Little MP, Azizova TV, Bazyka D, Bouffler SD, Cardis E, Chekin S, et al. Systematic review and meta-analysis of circulatory disease from exposure to low-level ionizing radiation and estimates of potential population mortality risks. Environ Health Perspect 2012; 120:1503–11.
5. Yamada M, Wong FL, Fujiwara S, Akahoshi M, Suzuki G. Noncancer disease incidence in atomic bomb survivors, 1958–1998. Radiat Res 2004; 161:622–32.
6. Adams MJ, Grant EJ, Kodama K, Shimizu Y, Kasagi F, Suyama A, et al. Radiation dose associated with renal failure mortality: A potential pathway to partially explain increased cardiovascular disease mortality observed after whole-body irradiation. Radiat Res 2012; 177:220–8.
7. Sera N, Hida A, Imaizumi M, Nakashima E, Akahoshi M. The association between chronic kidney disease and cardiovascular disease risk factors in atomic bomb survivors. Radiat Res 2013; 179:46–52.
8. Baker JE, Fish BL, Su J, Haworth ST, Strande JL, Komorowski RA, et al. 10 Gy total body irradiation increases risk of coronary sclerosis, degeneration of heart structure and function in a rat model. Int J Rad Biol 2009; 85:1089–100.
9. Lenarczyk M, Lam V, Jensen E, Fish BL, Su J, Koprowski S, et al. Cardiac injury after 10 Gy total body irradiation: Indirect role of effects on abdominal organs. Radiat Res 2013; 180:247–58.
10. Shimizu Y, Kodama K, Nishi N, Kasagi F, Suyama A, Soda M, et al. Radiation exposure and circulatory disease risk: Hiroshima and Nagasaki atomic bomb survivor data, 1950–2003. BMJ (Clinical Research Ed) 2010; 340:b5349.
11. Zhao W, Robbins ME. Inflammation and chronic oxidative stress in radiation-induced late normal tissue injury: Therapeutic implications. Curr Med Chem 2009; 16:130–43.
12. Robbins MEC, Zhao W. Chronic oxidative stress and radiation-induced late normal tissue injury: A review. Int J Rad Biol 2004; 80:251–9.
13. Fajardo LF, Berthrong M. Vascular lesions following radiation. Pathol Annu 1988; 23 Pt 1:297–330.
14. Gaugler MH. A unifying system: Does the vascular endothelium have a role to play in multi-organ failure following radiation exposure? BJR Supplement 2005; 27:100–5.
15. Satyamitra MM, DiCarlo AL, Taliaferro L. Understanding the pathophysiology and challenges of development of medical countermeasures for radiation-induced vascular/endothelial cell injuries: Report of a NIAID workshop, August 20, 2015. Radiat Res 2016; 186:99–111.
16. Dong X, Tong F, Qian C, Zhang R, Dong J, Wu G, et al. Nemo modulates radiation-induced endothelial senescence of human umbilical veins through NF-kappaB signal pathway. Radiat Res 2014; 183:82–93.
17. Wang Y, Boerma M, Zhou D. Ionizing radiation-induced endothelial cell senescence and cardiovascular diseases. Radiat Res 2016; 186:153–61.
18. Cohen EP, Fish BL, Irving AA, Rajapurkar MM, Shah SV, Moulder JE. Radiation nephropathy is not mitigated by antagonists of oxidative stress. Radiat Res 2009; 172:260–4.
19. Cohen EP, Lenarczyk M, Fish BL, Jia S, Hessner MJ, Moulder JE. Evaluation of genomic evidence for oxidative stress in experimental radiation nephropathy. J Genet Disor Genet Rep 2013; 2.

20. Unthank JL, Miller SJ, Quickery AK, Ferguson EL, Wang M, Sampson CH, et al. Delayed effects of acute radiation exposure in a murine model of the H-ARS: Multiple-organ injury consequent to less than 10 Gy total body irradiation. Health Phys 2015; 109:511–21.

21. Plett PA, Sampson CH, Chua HL, Joshi M, Booth C, Gough A, et al. Establishing a murine model of the hematopoietic syndrome of the acute radiation syndrome. Health Phys 2012; 103:343–55.

22. Sieber F, Muir SA, Cohen EP, Fish BL, Mäder M, Schock AM, et al. Dietary selenium for the mitigation of radiation injury: Effects of selenium dose escalation and timing of supplementation. Radiat Res 2011; 176:366–74.

23. Farris AB, Adams CD, Brousaides N, Della Pelle PA, Collins AB, Moradi E, et al. Morphometric and visual evaluation of fibrosis in renal biopsies. J Am Soc Nephrol 2011; 22:176–86.

24. Unthank JL, Fath SW, Burkhart HM, Miller S, Dalsing MC. Wall remodeling during luminal expansion of mesenteric arterial collaterals in the rat. Circ Res 1996; 79:1015–23.

25. Miller SJ, Watson WC, Kerr KA, Labarrere CA, Chen NX, Deeg MA, et al. Development of progressive aortic vasculopathy in a rat model of aging. Am J Physiol Heart Circ Physiol 2007; 293:H2634–43.

26. Schipke J, Brandenberger C, Rajces A, Manninger M, Alogna A, Post H, et al. Assessment of cardiac fibrosis: A morphometric method comparison for collagen quantification. J Appl Physiol (1985) 2017; 122:1019–30.

27. Seemann I, Gabriels K, Visser NL, Hoving S, te Poele JA, Pol JF, et al. Irradiation induced modest changes in murine cardiac function despite progressive structural damage to the myocardium and microvasculature. Radiother Oncol 2012; 103:143–50.

28. Moulder JE, Fish BL, Cohen EP. Treatment of radiation nephropathy with ACE inhibitors. Int J Radiat Oncol Biol Phys 1993; 27:93–9.

29. Glatstein E, Fajardo LF, Brown JM. Radiation injury in the mouse kidney. I. Sequential light microscopic study. Int J Radiat Oncol Biol Phys 1977; 2:933–43.

30. Robbins ME, Wooldridge MJ, Jaenke RS, Whitehouse E, Golding SJ, Rezvani M, et al. A morphological study of radiation nephropathy in the pig. Radiat Res 1991; 126:317–27.

31. Fonkalsrud EW, Sanchez M, Zerubavel R, Mahoney A. Serial changes in arterial structure following radiation therapy. Surg Gynecol Obstet 1977; 145:395–400.

32. Himmel PD, Hassett JM. Radiation-induced chronic arterial injury. Semin Surg Oncol 1986; 2:225–47.

33. Boerma M, Zurcher C, Esveldt I, Schutte-Bart CI, Wondergem J. Histopathology of ventricles, coronary arteries and mast cell accumulation in transverse and longitudinal sections of the rat heart after irradiation. Oncol Rep 2004; 12:213–9.

34. Lauk S. Endothelial alkaline phosphatase activity loss as an early stage in the development of radiation-induced heart disease in rats. Radiat Res 1987; 110:118–28.

35. Fajardo LF, Stewart JR. Capillary injury preceding radiation-induced myocardial fibrosis. Radiology 1971; 101:429–33.

36. Alfrey AC. Role of iron and oxygen radicals in the progression of chronic renal failure. Am J Kidney Dis 1994; 23:183–7.

37. Howard RL, Buddington B, Alfrey AC. Urinary albumin, transferrin and iron excretion in diabetic patients. Kidney Int 1991; 40:923–6.

38. Alfrey AC, Froment DH, Hammond WS. Role of iron in the tubulo-interstitial injury in nephrotoxic serum nephritis. Kidney Int 1989; 36:753–9.

39. Kamanna VS, Ganji SH, Shelkovnikov S, Norris K, Vaziri ND. Iron sucrose promotes endothelial injury and dysfunction and monocyte adhesion/infiltration. Am J Nephrol 2012; 35:114–9.

40. Woollard KJ, Sturgeon S, Chin-Dusting JPF, Salem HH, Jackson SP. Erythrocyte hemolysis and hemoglobin oxidation promote ferric chloride-induced vascular injury. J Biol Chem 2009; 284:13110–8.

41. Sahlstedt L, Ebeling F, Von Bonsdorff L, Parkkinen J, Ruutu T. Non-transferrin-bound iron during allogeneic stem cell transplantation. Br J Haematol 2001; 113:836–8.

42. Zhang X-H, Lou Z-X, Wang A-L, Hu X-D, Zhang H-Q. Development of serum iron as a biological dosimeter in mice. Radiat Res 2013; 179:684–9.

43. Xie LH, Zhang XH, Hu XD, Min XY, Zhou QF, Zhang HQ. Mechanisms of an increased level of serum iron in gamma-irradiated mice. Radiat Environ Biophys 2016; 55:81–8.

44. Sponsel HT, Alfrey AC, Hammond WS, Durr JA, Ray C, Anderson RJ. Effect of iron on renal tubular epithelial cells. Kidney Int 1996; 50:436–44.

45. Xie Y, Hou W, Song X, Yu Y, Huang J, Sun X, et al. Ferroptosis: Process and function. Cell Death Differ 2016; 23:369–79.

46. Fajardo LF. The complexity of endothelial cells. A review. Am J Clin Pathol 1989; 92:241–50.

47. Down JD, Berman AJ, Warhol M, Yeap B, Mauch P. Late complications following total-body irradiation and bone marrow rescue in mice: Predominance of glomerular nephropathy and hemolytic anemia. Int J Rad Biol 1990; 57:551–65.

48. Tapio S. Pathology and biology of radiation-induced cardiac disease. J Radiat Res 2016; 57:439–48.

49. Azimzadeh O, Sievert W, Sarioglu H, Merl-Pham J, Yentrapalli R, Bakshi MV, et al. Integrative proteomics and targeted transcriptomics analyses in cardiac endothelial cells unravel mechanisms of long-term radiation-induced vascular dysfunction. J Proteome Res 2015; 14:1203–19.

50. Chang J, Wang Y, Shao L, Laberge RM, Demaria M, Campisi J, et al. Clearance of senescent cells by ABT263 rejuvenates aged hematopoietic stem cells in mice. Nat Med 2016; 22:78–83.

51. Krishnamurthy J, Torrice C, Ramsey MR, Kovalev GI, Al-Regaiey K, Su L, et al. Ink4a/Arf expression is a biomarker of aging. J Clin Invest 2004; 114:1299–307.

52. Richardson RB. Ionizing radiation and aging: Rejuvenating an old idea. Aging (Albany NY) 2009; 1:887–902.

53. Halle M, Gabrielsen A, Paulsson-Berne G, Gahm C, Agardh HE, Farnebo F, et al. Sustained inflammation due to nuclear factor-kappa B activation in irradiated human arteries. J Am Coll Cardiol 2010; 55:1227–36.

54. Cohen EP, Hankey KG, Bennett AW, Farese AM, Parker GA, MacVittie TJ. Acute and chronic kidney injury in a non-human primate model of partial-body irradiation with bone marrow sparing. Radiat Res 2017; 188:661–71

55. Jaenke RS, Phemister RD, Norrdin RW. Progressive glomerulosclerosis and renal failure following perinatal gamma radiation in the beagle. Lab Invest 1980; 42:643–55.

56. Riley PA. Free radicals in biology: Oxidative stress and the effects of ionizing radiation. Int J Radiat Biol 1994; 65:27–33.

57. Lenarczyk M, Cohen EP, Fish BL, Irving AA, Sharma M, Driscoll CD, et al. Chronic oxidative stress as a mechanism for radiation nephropathy. Radiat Res 2009; 171:164–72.

58. Belin de Chantemele EJ, Vessieres E, Dumont O, Guihot AL, Toutain B, Loufrani L, et al. Reactive oxygen species are necessary for high flow (shear stress)-induced diameter enlargement of rat resistance arteries. Microcirculation 2009; 16:391–402.

59. Castier Y, Brandes RP, Leseche G, Tedgui A, Lehoux S. P47phox-dependent NADPH oxidase regulates flow-induced vascular remodeling. Circ Res 2005; 97:533–40.

60. Distasi MR, Unthank JL, Miller SJ. Nox2 and p47phox modulate compensatory growth of primary collateral arteries. Am J Physiol Heart Circ Physiol 2014; 306:H1435–43.

61. Griendling KK, Sorescu D, Ushio-Fukai M. NAD(P)H oxidase:

Role in cardiovascular biology and disease. Circ Res 2000; 86:494–501.

62. Loffredo L, Carnevale R, Cangemi R, Angelico F, Augelletti T, Di Santo S, et al. Nox2 up-regulation is associated with artery dysfunction in patients with peripheral artery disease. Int J Cardiol 2012; 165:184–92.

63. Violi F, Pignatelli P, Pignata C, Plebani A, Rossi P, Sanguigni V, et al. Reduced atherosclerotic burden in subjects with genetically determined low oxidative stress. Arterioscler Thromb Vasc Biol 2013; 33:406–12.

64. Murdoch CE, Chaubey S, Zeng L, Yu B, Ivetic A, Walker SJ, et al. Endothelial nadph oxidase-2 promotes interstitial cardiac fibrosis and diastolic dysfunction through proinflammatory effects and endothelial-mesenchymal transition. J Am Coll Cardiol 2014; 63:2734–41.

65. Sedeek M, Nasrallah R, Touyz RM, Hebert RL. NADPH oxidases, reactive oxygen species, and the kidney: Friend and foe. J Am Soc Nephrol 2013; 24:1512–8.

66. Wang Y, Liu L, Pazhanisamy SK, Li H, Meng A, Zhou D. Total body irradiation causes residual bone marrow injury by induction of persistent oxidative stress in murine hematopoietic stem cells. Free Radic Biol Med 2010; 48:348–56.

67. Freed JK, Beyer AM, LoGiudice JA, Hockenberry JC, Gutterman DD. Ceramide changes the mediator of flow-induced vasodilation from nitric oxide to hydrogen peroxide in the human microcirculation. Circ Res 2014; 115:525–32.

68. Dikalov S. Cross talk between mitochondria and NADPH oxidases. Free Radic Biol Med 2011; 51:1289–301.

69. Castier Y, Ramkhelawon B, Riou S, Tedgui A, Lehoux S. Role of NF-kappaB in flow-induced vascular remodeling. Antioxid Redox Signal 2009; 11:1641–9.